

**SUPPLEMENTARY INFORMATION FOR
“MACROSCOPIC QUANTUM TEST WITH BULK ACOUSTIC WAVE RESONATORS”**

Supplementary Section A: Geometric factor

The considered macrorealistic modifications lead to momentum diffusion in the oscillator state. The momentum diffusion rate $D = \hbar^2 U / \tau_e$ is inversely proportional to the coherence time parameter τ_e and depends on the oscillator mode function $\mathbf{u}(\mathbf{r})$ through the geometric factor [17]

$$U = \frac{1}{2\hbar^2} \int d^3q g(\mathbf{q}, \sigma_q) |\tilde{\mathbf{u}}(\mathbf{q}) \cdot \mathbf{q}|^2, \quad \text{with} \quad \tilde{\mathbf{u}}(\mathbf{q}) = \frac{1}{m_e} \int d^3r \varrho(\mathbf{r}) \mathbf{u}(\mathbf{r}) e^{-\mathbf{r} \cdot \mathbf{q}/\hbar}. \quad (\text{A1})$$

Here, m_e denotes the reference electron mass, and $g(\mathbf{q}, \sigma_q) = \exp(-|\mathbf{q}|^2/2\sigma_q^2)/(2\pi\sigma_q^2)^{3/2}$ a Gaussian momentum distribution of standard deviation σ_q . The resonator mode employed in this work can be modelled to great accuracy with the function

$$\mathbf{u}(\mathbf{r}) = \mathcal{N} e^{-(y^2+z^2)/w_0^2} \cos\left(\pi \frac{\ell x}{L}\right) \mathbf{e}_x, \quad (\text{A2})$$

where w_0 is the beam waist ($1/e$ amplitude radius), L is the height, and ℓ the mode index. Based on this mode function, we can define an effective mode volume and mass, $V_{\text{eff}} = \int d^3r |\mathbf{u}(\mathbf{r})|^2$ and $m_{\text{eff}} = \int d^3r \varrho(\mathbf{r}) |\mathbf{u}(\mathbf{r})|^2$. They both depend on the square of the amplitude prefactor \mathcal{N} , but the relevant physical displacement amplitudes of the individual atoms, $x_0 \mathbf{u}(\mathbf{r}_n) = \sqrt{\hbar/m_{\text{eff}} \omega} \mathbf{u}(\mathbf{r}_n)$, as well as the dimensionless macrorealistic diffusion rate, $\Gamma \tau_e = D(x_0/\hbar)^2 = U x_0^2$, do not depend on \mathcal{N} . Hence we may set $\mathcal{N} = 1$, without loss of generality, as done in the main text.

Given that we consider a displacement field with only a longitudinal component in x -direction, $\mathbf{u}(\mathbf{r}) = u_x(\mathbf{r}) \mathbf{e}_x$, and that the mass density distribution is assumed to be uniform (*i.e.* $\varrho(\mathbf{r}) = \bar{\varrho}$), Eq. (A1) can be simplified further:

$$\begin{aligned} U &= \frac{1}{2\hbar^2} \int d^3q g(\mathbf{q}, \sigma_q) |\tilde{u}_x(\mathbf{q}) q_x|^2 = \frac{\bar{\varrho}^2}{2\hbar^2 m_e^2} \int d^3q g(\mathbf{q}, \sigma_q) q_x^2 \left| \int dy dz e^{-i(q_y y + q_z z)/\hbar - (y^2+z^2)/w_0^2} \int_0^L dx \cos\left(\pi \frac{\ell x}{L}\right) e^{-iq_x x/\hbar} \right|^2 \\ &= \frac{\bar{\varrho}^2 \pi^2 w_0^4 L^2}{2\hbar^2 m_e^2} \int d^3q g(\mathbf{q}, \sigma_q) q_x^2 e^{-(q_y^2+q_z^2)w_0^2/2\hbar^2} \left| \int_0^1 d\phi \cos(\pi \ell \phi) e^{-i\phi q_x L/\hbar} \right|^2. \end{aligned} \quad (\text{A3})$$

This allows us to first integrate out the momenta \mathbf{q} , change to cylindrical coordinates and express the end result as

$$U = \frac{\bar{\varrho}^2}{2m_e^2} \frac{\pi^2 w_0^4}{1 + \sigma_w^2} \int d\zeta \frac{\zeta^2}{\sqrt{2\pi\sigma_L}} e^{-\zeta^2/2\sigma_L^2} \left| \int_0^1 d\phi \cos(\pi \ell \phi) e^{-i\phi \zeta} \right|^2 = \frac{\bar{\varrho}^2 \pi^2 w_0^4}{m_e^2 (1 + \sigma_w^2)} \int d\zeta \frac{e^{-\zeta^2/2\sigma_L^2}}{\sqrt{2\pi\sigma_L}} \frac{1 - (-)^{\ell} \cos \zeta}{\left(1 - \frac{\pi^2 \ell^2}{\zeta^2}\right)^2}. \quad (\text{A4})$$

with $\sigma_L = L\sigma_q/\hbar$ and $\sigma_w = w_0\sigma_q/\hbar$. Once we identify $m_{\text{eff}} = \bar{\varrho}\pi w_0^2 L/4$, we arrive at the expression for the diffusion rate $\Gamma = U x_0^2 / \tau_e$ given in the main text. A non-tight upper bound follows by pulling the absolute value into the ϕ -integral in (A4). The ϕ -integral then evaluates to $2/\pi$, so that $U < 2\bar{\varrho}^2 w_0^4 \sigma_L^2 / m_e^2 (1 + \sigma_w^2)$, and $\Gamma < (32/\pi^2)(m_{\text{eff}}^2/m_e^2 \tau_e)(\sigma_q x_0/\hbar)^2 / (1 + \sigma_w^2)$. The scaling of this bound with the mode mass and geometry is deceptively similar to previous results for center-of-mass oscillations. However, we will see in the following that the bound is rather loose and the actual diffusion rate for bulk acoustic modes exhibits a completely different scaling.

In the limiting case $\sigma_L, \sigma_w \ll 1$, the Gaussian function is sharply peaked around $\zeta = 0$, and we can expand the remainder of the integrand to lowest non-vanishing order; for even ℓ , this yields $U \approx 15\bar{\varrho}^2 w_0^4 \sigma_L^6 / 2\pi^2 m_e^2 \ell^4$, and $\Gamma \approx 120(m_{\text{eff}}^2/m_e^2 \tau_e)(\sigma_q x_0/\hbar)^2 (\sigma_L/\pi \ell)^4$. For decreasing σ_q , this rate drops as σ_q^6 . Notice that odd ℓ would result in a σ_q^4 -scaling, $U \approx 3\bar{\varrho}^2 w_0^4 \sigma_L^4 / \pi^2 m_e^2 \ell^4$.

Greater care must be taken in the opposite limit, $\sigma_L, \sigma_w \gg 1$. Although the non-Gaussian part of the integrand in (A4) is clearly peaked around $\zeta = \pm\pi\ell$, it is asymptotically of order ζ^0 and thus non-integrable without the regularizing presence of the Gaussian. Hence a dominant contribution to the ζ -integral in (A4) does not come from the vicinity of the peaks, but from $|\zeta| \gg \pi\ell$. For even greater values $\sigma_L \gg \pi\ell$, we can approximate to lowest order

$$U \approx U^{(0)} := \frac{\bar{\varrho}^2 \pi^2 w_0^4}{m_e^2 (1 + \sigma_w^2)} \int d\zeta \frac{e^{-\zeta^2/2\sigma_L^2}}{\sqrt{2\pi\sigma_L}} [1 - (-)^{\ell} \cos \zeta] = \frac{\bar{\varrho}^2 \pi^2 w_0^4}{m_e^2 (1 + \sigma_w^2)} [1 - (-)^{\ell} e^{-\sigma_L^2/2}] \approx \frac{\bar{\varrho}^2 \pi^2 w_0^4}{m_e^2 \sigma_w^2}. \quad (\text{A5})$$

The corresponding diffusion rate reads as $\Gamma \approx 16(m_{\text{eff}}^2/m_e^2 \tau_e)(x_0/\sigma_L w_0)^2$, which does not depend on ℓ , is proportional to m_{eff} , and is again monotonic in σ_q . In order to access the most relevant intermediate σ_q -regime of maximum diffusion, consider the

correction $U = U^{(0)} + U^{(1)}$, which can be expressed as

$$U^{(1)} = \frac{\bar{\varrho}^2 \pi^4 \ell^2 w_0^4}{m_e^2 (1 + \sigma_w^2)} \int d\zeta \frac{e^{-\zeta^2/2\sigma_L^2}}{\sqrt{2\pi}\sigma_L} \left[\frac{2\zeta^2 - \pi^2 \ell^2}{2(\zeta + \pi\ell)^2} \text{sinc}^2 \left(\frac{\zeta - \pi\ell}{2} \right) \right]. \quad (\text{A6})$$

The non-Gaussian part of this integrand (square-bracketed) is not only sharply peaked at $\zeta = \pm\pi\ell$, but also asymptotically converges to zero like ζ^{-2} . The integral of this expression evaluates to $\pi/2$. Assuming $\pi\ell \gg 1$, we can now replace ζ^2 in the Gaussian by $\pi^2 \ell^2$, so that

$$U^{(1)} \approx \frac{\bar{\varrho}^2 \pi^5 \ell^2 w_0^4}{2m_e^2 (1 + \sigma_w^2)} \frac{e^{-\pi^2 \ell^2 / 2\sigma_L^2}}{\sqrt{2\pi}\sigma_L} \approx \frac{\bar{\varrho}^2 \pi^5 \ell^2 w_0^4 e^{-\pi^2 \ell^2 / 2\sigma_L^2}}{2\sqrt{2\pi} m_e^2 \sigma_w^2 \sigma_L}, \quad U \approx \frac{\bar{\varrho}^2 \pi^2 w_0^2 L^2}{m_e^2 \sigma_L^2} \left(1 + \frac{\pi^3 \ell^2 e^{-\pi^2 \ell^2 / 2\sigma_L^2}}{2\sqrt{2\pi}\sigma_L} \right) = \frac{16m_{\text{eff}}^2}{m_e^2 \sigma_L^2 w_0^2} \left(1 + \frac{\pi^3 \ell^2 e^{-\pi^2 \ell^2 / 2\sigma_L^2}}{2\sqrt{2\pi}\sigma_L} \right) \quad (\text{A7})$$

Presuming $\sigma_w \gg 1$, the local maximum of U coincides approximately with that of $U^{(1)}$, at $\sigma_L \approx \pi\ell / \sqrt{3}$. It marks the σ_q -value at which the experiment is most sensitive to macrorealistic diffusion. The maximum rate reads as

$$\max_{\sigma_q} \Gamma \approx \frac{48m_{\text{eff}}^2 x_0^2}{m_e^2 \tau_e \pi^2 \ell^2 w_0^2} \left(1 + \sqrt{\frac{3\pi}{8e^3}} \pi\ell \right)^{\pi\ell \gg 1} \approx \sqrt{\frac{3\pi}{2e^3}} \frac{24}{\pi\ell\tau_e} \left(\frac{m_{\text{eff}} x_0}{m_e w_0} \right)^2 = \sqrt{\frac{3\pi}{2e^3}} \frac{6\hbar\bar{\varrho}}{m_e^2 \omega \tau_e} \frac{L}{\ell}. \quad (\text{A8})$$

For numerical evaluation, an exact expression of the diffusion rate can be given in terms of

$$U = \frac{\bar{\varrho}^2}{2m_e^2} \frac{\pi^2 w_0^4 \sigma_L^2}{1 + \sigma_w^2} f_\ell(\sigma_L), \quad \text{with} \quad f_\ell(\xi) = (1 + \xi \partial_\xi) \int_{[0,1]^2} d\phi_1 d\phi_2 \cos \ell\pi\phi_1 \cos \ell\pi\phi_2 e^{-\xi^2(\phi_1 - \phi_2)^2/2}. \quad (\text{A9})$$

The function f_ℓ can be evaluated to

$$f_\ell(\sigma_L) = \frac{1}{\sqrt{2}\sigma_L^5} \left\{ -\ell\pi h(\sigma_L, 0, \ell) + \sqrt{2}\sigma_L \left[(-)^\ell e^{-\sigma_L^2/2} - 1 \right] (\ell^2 \pi^2 - 2\sigma_L^2) + (-)^\ell \ell \pi^2 \text{Re} [h(\sigma_L, \sigma_L, \ell)] \right\}, \quad (\text{A10})$$

where

$$h(a, b, \ell) = -i \frac{\sqrt{\pi}}{2} [6a^2 - 2\ell\pi(\ell\pi - ib^2)] \text{erf} \left[\frac{i(\ell\pi/a - ib)}{\sqrt{2}} \right] \exp \left[-\frac{(\ell\pi/a - ib)^2}{2} \right]. \quad (\text{A11})$$

In Fig. S3, we plot the resulting diffusion rate $\Gamma = D/\hbar m_{\text{eff}} \omega = \hbar U/m_{\text{eff}} \omega \tau_e$ as a function of the modification parameter σ_q . We compare the mode addressed in our experiment to one with a much lower frequency and mode index. Based on the above reasoning, the maxima are expected to be at $\hbar/\sigma_q \approx 0.5 \mu\text{m}$ ($\ell = 486$) and $17 \mu\text{m}$ ($\ell = 8$), which roughly agrees with the exact positions on the logarithmic scale. The dotted line represents $U^{(1)}$ from (A7), a good approximation in the relevant regime around maximum diffusion. The dashed lines show the asymptotic approximations for $\sigma_L \gg \pi\ell$ (left) and for $\sigma_L \ll 1$ (right).

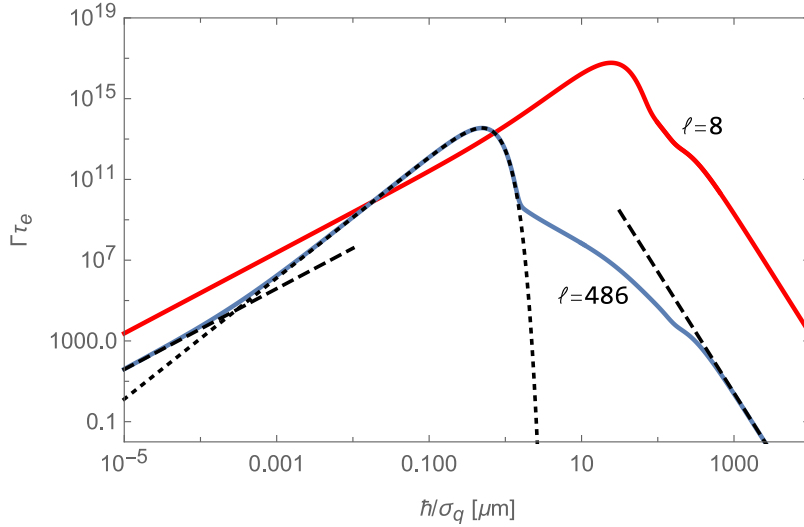


FIG. S3. Dimensionless diffusion rate $\Gamma\tau_e$ as function of the modification parameter σ_q for the device studied in the main text (blue curve). We compare it to the correction $U^{(1)}$ from (A7) (dotted line), as well as to the asymptote $U^{(0)}$ for $\sigma_L \gg \pi\ell$ (left dashed) and to the asymptote for $\sigma_L \ll 1$ (right dashed). Much stronger diffusion would arise (red curve) if instead of the mode at $\ell = 486$, we could excite, say, the mode with index $\ell = 8$ at the frequency $\omega = 2\pi \cdot 98$ MHz.

Supplementary Section B: Initial states and time evolution

In our setup, macrorealistic collapse models are put to the test by monitoring the decay of Fock and superposition states over a finite amount of time. To assess the influence of those models, it is convenient to solve the time evolution in the Wigner phase space representation of the oscillator state. The one-dimensional Wigner function is defined as

$$W(x, p) = \frac{1}{2\pi\hbar} \int ds e^{ips/\hbar} \langle x - s/2 | \rho | x + s/2 \rangle, \quad (\text{B1})$$

where x and p are the position and momentum coordinates of the harmonic oscillator. For better readability we now change to dimensionless units $X = \sqrt{m_{\text{eff}}\omega/\hbar}x$ and $P = \sqrt{\hbar/m_{\text{eff}}\omega}p$. Then the Wigner functions (B1) of the ground state $|0\rangle$, first excited Fock state $|1\rangle$, and the superposition state $(|0\rangle + |1\rangle)/\sqrt{2}$, respectively, read as

$$W_0(X, P) = \frac{1}{\pi} e^{-X^2 - P^2}, \quad W_1(X, P) = \frac{1}{\pi} [2X^2 + 2P^2 - 1] e^{-X^2 - P^2}, \quad \text{and} \quad W_{10}(X, P) = \frac{1}{2\pi} [(1 + \sqrt{2}X)^2 - 1 + 2P^2] e^{-X^2 - P^2}. \quad (\text{B2})$$

The time evolution of the state described by the master equation (6) in the main text describes the impact of the macrorealistic diffusion at the rate Γ , averaged over the free oscillation, and it includes also an environmental decay channel at the rate γ_{\downarrow} . The two separate Lindblad generators for decay and amplification, $\partial_t^{\text{dec}}\rho = \Gamma\mathcal{D}[\mathbf{a}]\rho$ and $\partial_t^{\text{amp}}\rho = \Gamma\mathcal{D}[\mathbf{a}^{\dagger}]\rho$ with $\mathbf{a} = (X + iP)/\sqrt{2}$, translate into phase space as

$$\partial_t^{\text{dec}} W(X, P) = \frac{\Gamma}{2\pi} \int ds e^{ips} \langle X - s/2 | \mathbf{a} \rho \mathbf{a}^{\dagger} - \frac{1}{2} \{ \mathbf{a}^{\dagger} \mathbf{a}, \rho \} | X + s/2 \rangle = \frac{\Gamma}{4} [\partial_X^2 + \partial_P^2 + 2\partial_X X + 2\partial_P P] W(X, P), \quad (\text{B3})$$

$$\partial_t^{\text{amp}} W(X, P) = \frac{\Gamma}{4} [\partial_X^2 + \partial_P^2 - 2\partial_X X - 2\partial_P P] W(X, P). \quad (\text{B4})$$

Both are classical Fokker-Planck equations, and the first one describes thermalization at the (dimensionless) energy $1/2$, *i.e.* the ground state energy of the quantum oscillator. The master equation then yields

$$\partial_t W(X, P) = \frac{\Gamma}{2} [\partial_X^2 + \partial_P^2] + \frac{\gamma_{\downarrow}}{4} [\partial_X^2 + \partial_P^2 + 2\partial_X X + 2\partial_P P] W(X, P). \quad (\text{B5})$$

The solution to this Fokker-Planck equation is obtained with help of a Fourier transform into the characteristic function representation,

$$\chi(x, p) = \int dx' dp' W(x', p') e^{i(xp' - p'x')/\hbar}, \quad (\text{B6})$$

which evolves according to

$$\partial_t \chi(X, P) = \frac{1}{2} \left[- \left(\frac{\gamma_{\downarrow}}{2} + \Gamma \right) (X^2 + P^2) - \gamma_{\downarrow} (X \partial_X + P \partial_P) \right] \chi(X, P). \quad (\text{B7})$$

We can now separate the simple relaxation dynamics (an exponential contraction toward the origin) from the diffusion. Let $X = \tilde{X} e^{\gamma_{\downarrow} t/2}$, $P = \tilde{P} e^{\gamma_{\downarrow} t/2}$, and $\Phi(\tilde{X}, \tilde{P}; t) = \chi(\tilde{X} e^{\gamma_{\downarrow} t/2}, \tilde{P} e^{\gamma_{\downarrow} t/2}; t)$, which then obeys

$$\partial_t \Phi(\tilde{X}, \tilde{P}; t) = - \frac{\gamma_{\downarrow} + 2\Gamma}{4} e^{\gamma_{\downarrow} t} (\tilde{X}^2 + \tilde{P}^2) \Phi(\tilde{X}, \tilde{P}; t), \quad (\text{B8})$$

as solved by

$$\Phi(\tilde{X}, \tilde{P}; t) = \exp \left[- \left(1 + \frac{2\Gamma}{\gamma_{\downarrow}} \right) (e^{\gamma_{\downarrow} t} - 1) \frac{\tilde{X}^2 + \tilde{P}^2}{4} \right] \Phi(\tilde{X}, \tilde{P}; 0), \quad (\text{B9})$$

so that

$$\chi(X, P; t) = \exp \left[- \left(1 + \frac{2\Gamma}{\gamma_{\downarrow}} \right) (1 - e^{-\gamma_{\downarrow} t}) \frac{X^2 + P^2}{4} \right] \chi(X e^{-\gamma_{\downarrow} t/2}, P e^{-\gamma_{\downarrow} t/2}; 0). \quad (\text{B10})$$

From this expression it is evident that the time evolution of an initial $\chi(X, P; 0)$ is simply given by a multiplication with a Gaussian exponential combined with an isotropic rescaling of the arguments. Noting that $\chi(0, 0; t) = 1$ at any time, one can check that the asymptotic steady state is a Gaussian, $\chi(X, P; \infty) = \exp[-(1 + 2\Gamma/\gamma_{\downarrow})(X^2 + P^2)/4]$, which for $\Gamma = 0$ is the ground state of the harmonic oscillator.

Back in the Wigner representation, the solution turns into a rescaling combined with a Gaussian convolution. Introducing the dimensionless quantity $\tilde{T} = 1/2 + \Gamma/\gamma_{\downarrow}$, we get

$$\begin{aligned} W(X, P; t) &= \frac{1}{4\pi^2} \int d\tilde{X} d\tilde{P} e^{i\tilde{P}X - i\tilde{P}\tilde{X}} \exp \left[-\tilde{T}(1 - e^{-\gamma_{\downarrow} t}) \frac{\tilde{X}^2 + \tilde{P}^2}{2} \right] \chi(\tilde{X} e^{-\gamma_{\downarrow} t/2}, \tilde{P} e^{-\gamma_{\downarrow} t/2}; 0) \\ &= \frac{1}{4\pi^2} \int d\tilde{X} d\tilde{P} dX_0 dP_0 W(X_0, P_0; 0) \exp \left[-\tilde{T}(1 - e^{-\gamma_{\downarrow} t}) \frac{\tilde{X}^2 + \tilde{P}^2}{2} + i\tilde{X}(P_0 e^{-\gamma_{\downarrow} t/2} - P) - i\tilde{P}(X_0 e^{-\gamma_{\downarrow} t/2} - X) \right] \\ &= \frac{1}{2\pi\tilde{T}(1 - e^{-\gamma_{\downarrow} t})} \int dX_0 dP_0 W(X_0, P_0; 0) \exp \left[-\frac{(X - X_0 e^{-\gamma_{\downarrow} t/2})^2 + (P - P_0 e^{-\gamma_{\downarrow} t/2})^2}{2\tilde{T}(1 - e^{-\gamma_{\downarrow} t})} \right] \\ &= \frac{e^{\gamma_{\downarrow} t}}{2\pi\tilde{T}(1 - e^{-\gamma_{\downarrow} t})} \int dX_0 dP_0 W(X_0 e^{\gamma_{\downarrow} t/2}, P_0 e^{\gamma_{\downarrow} t/2}; 0) \exp \left[-\frac{(X - X_0)^2 + (P - P_0)^2}{2\tilde{T}(1 - e^{-\gamma_{\downarrow} t})} \right]. \end{aligned} \quad (\text{B11})$$

The two last lines are alternative ways to write the convolution. Given the simple Gaussian form of the initial Wigner functions (B2), the integrals can be calculated analytically and result in

$$W_0(X, P; t) = \frac{1}{\pi R(t)} \exp \left[\gamma_{\downarrow} t - \frac{e^{\gamma_{\downarrow} t} (X^2 + P^2)}{R(t)} \right], \quad (\text{B12})$$

$$W_1(X, P; t) = \frac{4\tilde{T}^2 + 2e^{\gamma_{\downarrow} t} (X^2 + P^2 + 2(e^{\gamma_{\downarrow} t} - 2)\tilde{T}^2) - 1}{\pi R^3(t)} \exp \left[\frac{\gamma_{\downarrow} t (1 - 2\tilde{T}) - e^{\gamma_{\downarrow} t} (X^2 + P^2 - 2\tilde{T}\gamma_{\downarrow} t)}{R(t)} \right], \quad (\text{B13})$$

$$\begin{aligned} W_{10}(X, P; t) &= \frac{\sqrt{8} e^{3\gamma_{\downarrow} t/2} X \tilde{T} + 4e^{2\gamma_{\downarrow} t} \tilde{T}^2 - \sqrt{2} e^{\gamma_{\downarrow} t/2} X (2\tilde{T} - 1) + 2\tilde{T} (2\tilde{T} - 1) + e^{\gamma_{\downarrow} t} (P^2 + X^2 + 2\tilde{T} - 8\tilde{T}^2)}{\pi R^3(t)} \\ &\quad \times \exp \left[\frac{\gamma_{\downarrow} t (1 - 2\tilde{T}) - e^{\gamma_{\downarrow} t} (X^2 + P^2 - 2\tilde{T}\gamma_{\downarrow} t)}{R(t)} \right], \end{aligned} \quad (\text{B14})$$

with $R(t) = 1 + 2(e^{\gamma_{\downarrow} t} - 1)\tilde{T}$. These expressions can be directly compared to the experimentally reconstructed Wigner function, which allows us to perform Bayesian parameter estimation of the macrorealistic Γ -values that are compatible with the measured data.

In Fig. S4, we use Eqs. (B13), (B14) to illustrate the evolution of states $|1\rangle$ and $(|0\rangle + |1\rangle)/\sqrt{2}$ according to either pure relaxation, pure diffusion, or a combination of both. Notice the significant differences in the dynamics between the different cases.

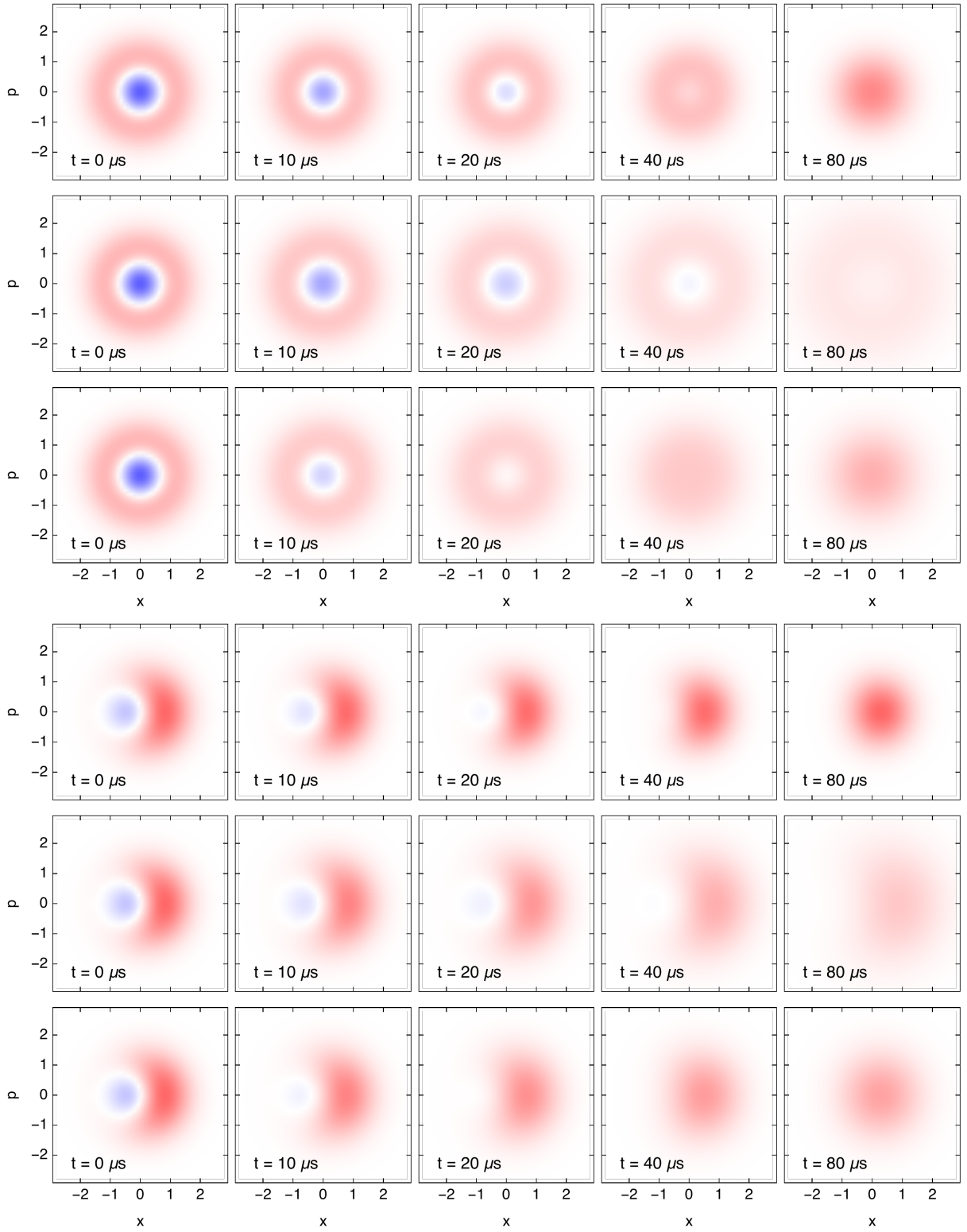


FIG. S4. Comparison between relaxation, diffusion, and a combination of both. Rows 1 and 4: State $|1\rangle$ and $(|0\rangle + |1\rangle)/\sqrt{2}$ evolved according to a relaxation process with $1/\gamma_1 = 40 \mu\text{s}$. Rows 2 and 5: same initial states, but evolved according to a purely dissipative process with $\Gamma = 10^4 \text{ Hz}$. Rows 3 and 6: evolution of the initial states according to a combination of both relaxation and diffusion with same rates. Note that in the actual experiment we have $\gamma_1 \gg \Gamma$, thus diffusion contributes very little compared to relaxation.

Supplementary Section C: Bayesian parameter estimation

By measuring the Wigner function at several instances of time and comparing it to the theoretical predictions in Sect. B, one can infer the most likely values for the macrorealistic diffusion rate Γ and, subsequently, for the values of the time parameter $\tau_e = \hbar U / \Gamma m_{\text{eff}} \omega$ by virtue of Bayes' rule. The posterior distribution of τ_e -values given the measured data d , a fixed value of the parameter σ_q , and an independently inferred decay time $1/\gamma_{\downarrow} \approx T_1$, updates as [17]

$$p(\tau_e|d; \sigma_q, T_1) \propto p(d|\tau_e; \sigma_q, T_1)p(\tau_e|\sigma_q, T_1), \quad (\text{C1})$$

Here, $d = [d_{ij}(t)]$ subsumes all recorded pixel values $d_{ij}(t) \in \mathbb{R}$ of the two-dimensional Wigner function reconstructions at the times $t = 10, 20, 40 \mu\text{s}$, as plotted in the main text. The likelihood $p(d|\tau_e; \sigma_q, T_1)$ for d follows from the theoretical model for the Wigner function evaluated at the recorded pixel coordinates and times, $W(X_i, P_j; t)$, and the assumption of additional Gaussian noise in each data point. That is, we model the likelihood for each pixel value by a Gaussian distribution of standard deviation s , so that

$$p(d|\tau_e; \sigma_q, T_1) = \prod_{i,j,t} \frac{1}{\sqrt{2\pi s^2}} \exp \left\{ -\frac{[d_{ij}(t) - W(X_i, P_j; t)]^2}{2s^2} \right\}. \quad (\text{C2})$$

We extract the overall noise level s by taking a sample of all pixel values for the Fock- $|1\rangle$ measurements at $t = 0, 10, 20, 40 \mu\text{s}$ and subtracting the respective model Wigner functions $W_1(X, P; t)$ with decay time T_1 and without macrorealistic diffusion ($\Gamma = 0$). A histogram of the resulting pixel deviations $\Delta_{ij}(t) = d_{ij}(t) - W_1(X_i, P_j; t)$ is shown in Fig. S5(a), together with a Gaussian fit that yields the noise level $s = 0.034$.

The prior $p(\tau_e|\sigma_q, T_1)$ is chosen as Jeffreys' prior [27], which is maximally objective and fair in a comparison with other completely different experiments [17]. It is defined as

$$p(\tau_e|\sigma_q, T_1) \propto \sqrt{I(\tau_e|\sigma_q, T_1)} = \sqrt{\left\langle \left(\frac{\partial}{\partial \tau_e} \log p(d|\tau_e; \sigma_q, T_1) \right)^2 \right\rangle_d}, \quad (\text{C3})$$

where $I(\tau_e|\sigma_q, T)$ is the Fisher information of the likelihood with respect to τ_e and $\langle \cdot \rangle_d$ denotes the expectation value over all possible measurement results, $d_{ij}(t) \in \mathbb{R}$.

We perform the Bayesian update (C1) with the data obtained for the three time snapshots at 10, 20, 40 μs . Figures S5(b) and (c) show the resulting posterior distributions over Γ -values for the Fock- $|1\rangle$ and the superposition state, respectively. The upper five-percent quantiles for Γ , marked by vertical lines, correspond to lower five-percent quantiles of $\tau_e = \hbar U / \Gamma m_{\text{eff}} \omega$ at a given value for σ_q . Smaller time parameters are thus ruled out with 95% confidence. We find the threshold values of $\Gamma = 1.6 \cdot 10^2 \text{ s}^{-1}$ and $6.4 \cdot 10^2 \text{ s}^{-1}$ in (b) and (c), respectively. More conservatively, the respective bounds would be $\Gamma = 3.1 \cdot 10^2 \text{ s}^{-1}$ and $8.3 \cdot 10^2 \text{ s}^{-1}$ at the confidence level $1 - 10^{-3}$ (roughly corresponding to 3σ for normally distributed estimates), or $\Gamma = 5.5 \cdot 10^2 \text{ s}^{-1}$ and $1.1 \cdot 10^3 \text{ s}^{-1}$ at the confidence level $1 - 10^{-7}$ (roughly 5σ). We attribute the greater threshold value in the superposition measurement to the omitted influence of environmental dephasing, which occurs at a comparable rate of $1/T_\phi = 1.0 \cdot 10^3 \text{ s}^{-1}$, as discussed in the main text. The remaining discrepancy between this rate and the inferred Γ can be explained by the different impact of diffusion and pure dephasing on the oscillator state.

In order to obtain the macroscopicity values, we take the maximum of the ruled out τ_e -range over σ_q , which coincides with the local maximum of the dimensionless diffusion rate at $\hbar/\sigma_q = 0.5 \mu\text{m}$, as depicted in Fig. S3. Employing the same 95% confidence level as in previous assessments, this leads to the macroscopicity values $\mu = 11.3$ and 10.7 for the two measured states.

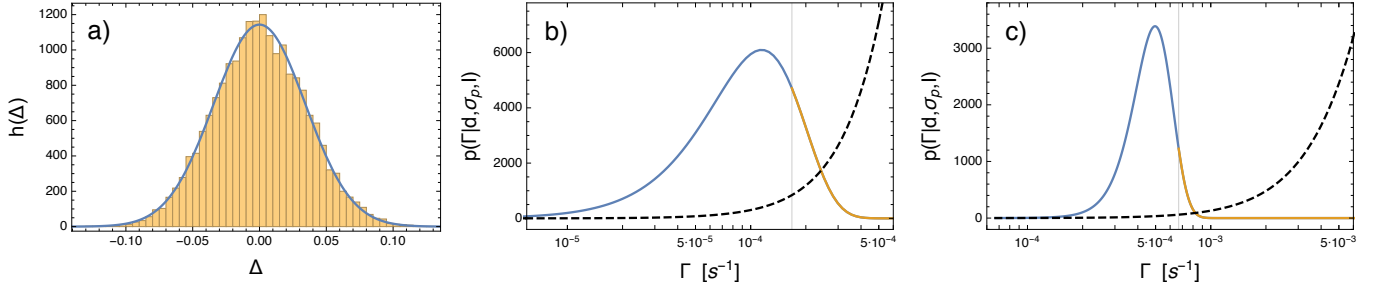


FIG. S5. Bayesian inference of the diffusion rate. (a): Histogram of pixel deviations $\Delta_{ij}(t)$ between recorded data and model Wigner function, sampled from four time snapshots of the Fock state measurement. The histogram is closely matched by a Gaussian fit (solid line) with standard deviation $s = 0.034$. (b): Posterior distribution for the diffusion rate Γ for the single Fock state data up at $t = 10, 20, 40 \mu\text{s}$. For comparison, the dashed curve depicts Jeffreys' prior, which has been updated by the posterior toward significantly lower Γ -values. The use of Jeffreys' prior leads to a more conservative estimate of excluded Γ -values than, say, the often used flat prior. The vertical line and the yellow part mark the upper five percent quantile of the posterior. (c) Posterior distribution for the superposition state data.

Supplementary Section D: Macroscopicity estimates for other mechanical resonators

We report here the parameters used to estimate the macroscopicities reachable in the two other reported experiments with mechanical resonators, where Wigner function negativities have been measured in the initial state [12, 13]. These experiments involve resonators with acoustic modes of complicated geometry [28, 29], so that it is not easy to derive simple analytical expressions as for the Laguerre-Gaussian modes we considered. For this reason, we proceed with making a conservative analysis, based on approximating such devices to cuboids hosting a sinusoidal displacement field, $u(\mathbf{r}) = \cos(\pi/h) \mathbf{e}_x$ with h the longitudinal extension of the mode. This yields an analytic expression for the geometric factor (A1) determining macrorealistic diffusion, which would otherwise require numerical integration of the displacement field resulting from a finite-element simulation of the actual device. Our approximation is conservative in the sense that it likely overestimates the effective oscillator mass, but we do not expect it to result in macroscopicities that deviate much from the actual one (given that μ is in logarithmic scale).

The experiments in Refs. [12, 13] show measurements of Wigner function negativities with the sake of demonstrating nonclassical state preparation, but they do not monitor the disappearance of such quantum features with time. We can therefore merely estimate the potential of these setups to perform a test of macrorealist models from the limitations imposed by the reported T_1 -times. To this end, we simply assume that our data were obtained with their resonators at the same *relative* times t/T_1 , which amounts to rescaling our inferred Γ -values by the ratio between our T_1 time and theirs.

Phononic crystal resonator Ref. [13]: We consider a phonon mode with frequency $\omega = 2\pi \cdot 2 \text{ GHz}$, wavelength $\lambda = 1 \mu\text{m}$, and decay time $T_1 = 1 \mu\text{s}$. The resonator itself is approximated by a lithium niobate (density 4.65 g cm^{-3}) cuboid of size $1 \times 1 \times 0.25 \mu\text{m}$ and total mass $m = 1.16 \cdot 10^{-15} \text{ kg}$, with an effective mass of $m_{\text{eff}} = 5.8 \cdot 10^{-16} \text{ kg}$. We assume a hypothetical experiment that excludes diffusion rates $\Gamma > 13.7 \text{ kHz}$, which results in $\mu = 9.0$ after maximizing with respect to σ_q .

Surface acoustic waves Ref. [12]: We consider a phonon mode with frequency $\omega = 2\pi \cdot 4 \text{ GHz}$, wavelength $\lambda = 1 \mu\text{m}$, and decay time $T_1 = 150 \text{ ns}$. The resonator is approximated by a lithium niobate (density 4.65 g cm^{-3}) cuboid of size [30] $75 \times 50 \times 1 \mu\text{m}$, with total mass $m = 1.744 \cdot 10^{-11} \text{ kg}$ and effective mass $m_{\text{eff}} = 8.7 \cdot 10^{-12} \text{ kg}$. The hypothetical experiment would exclude $\Gamma > 91.5 \text{ kHz}$, resulting in $\mu = 8.6$.

Supplementary Section E: Experimental sequences

1. Phonon mode characterization

To characterize the phonon mode under investigation, we perform two standard measurements [31]. The first is a population decay (“ring-down”) measurement, which gives the relaxation rate $1/T_1$. This is done by preparing the phonon mode in Fock state $|1\rangle$, and then monitoring its population decay over time, see Fig. (S6). Fitting the measured data with a decaying exponential e^{-t/T_1} plus a constant background gives us the time parameter $T_1 = 85.8 \pm 1.5 \mu\text{s}$, where the error is one standard deviation given by the fitting function. In the assumed model (6), the measured relaxation rate corresponds to $1/T_1 = 2\Gamma + \gamma_l$.

The second measurement consists of a Ramsey sequence, which monitors dephasing effects. This is done by preparing the phonon mode in state $(|0\rangle + |1\rangle)/2$, and then monitoring its phase evolution over time, see Fig. (S6). Fitting the measured data to an exponentially decaying oscillation gives us the time constant $T_2 = 147.3 \pm 2.6 \mu\text{s}$, where the error is one standard deviation given by the fitting function. As this contrast reduction is partially due to the relaxation effect previously investigated,

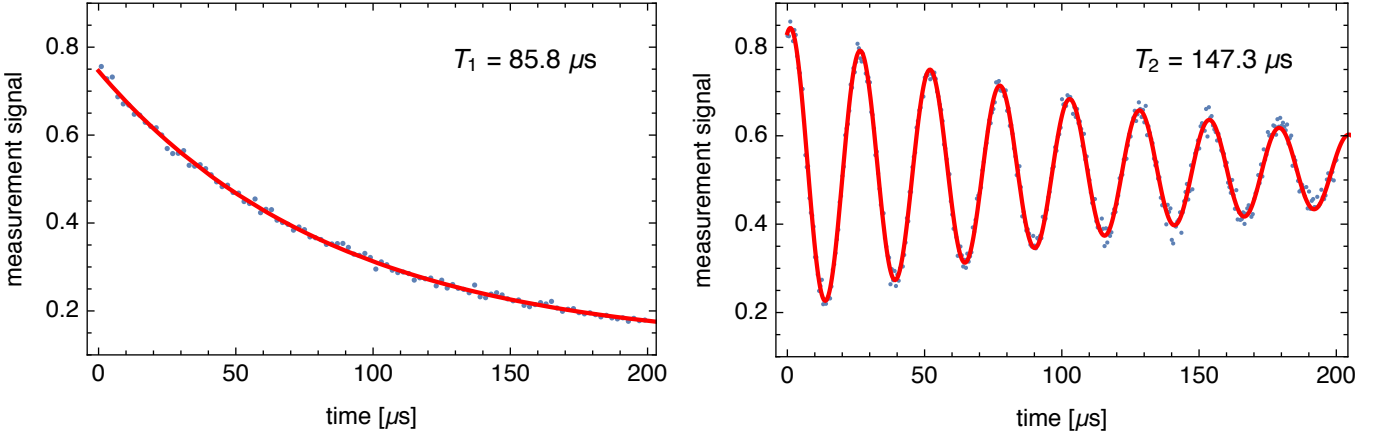


FIG. S6. Characterization of phonon coherence. Left: population decay measurement used to estimate the relaxation time T_1 . Right: phonon Ramsey measurement used to estimate the dephasing time T_2 .

it is convenient to identify the pure dephasing time as $T_\phi = (1/T_2 - 1/(2T_1))^{-1} = 1.0 \pm 0.2$ ms. This pure dephasing could be described by a Lindblad generator of the form $2\mathcal{D}[a^\dagger a]/T_\phi$.

We can also estimate the ground state population and the effective temperature of the phonon mode, which can be used for a classical noise test of macrorealistic collapse models. To this end, we tune the qubit frequency to be 0.8 MHz below the one of the phonon mode, operating our system in the strongly dispersive regime [14]. In this regime, the qubit frequency depends on the phonon mode occupation number, and therefore on its effective temperature. In Fig. S7 we present a spectroscopic measurement of the qubit frequency with the phonon mode in the stationary state, showing a prominent peak at the bare qubit frequency. From the data it is possible to note a slight asymmetry between the left and right tails of the peak, which is highlighted by comparing to a Voigt profile fit (blue line). This is expected at finite temperature, as any population in higher Fock states will result in additional peaks on the left-hand side of the main one. As the position of the peak for $|1\rangle$ is known, we fit again the data with a sum of two Voigt profiles of fixed frequencies (red dashed line). From the relative amplitude between the two peaks we estimate the thermal population of the 1-phonon excited state to be 1.6 ± 0.2 %. In our model (6) in the main text, this small population corresponds to $\Gamma/(2\Gamma + \gamma_\downarrow)$ to a good approximation. Hence $\Gamma \ll \gamma_\downarrow$, and we can safely identify the measured relaxation rate with the model rate, $\gamma_\downarrow \approx 1/T_1$, within the uncertainty of the fit.

2. State preparation and read-out

To acquire the data presented in Fig. 2 of the main text, we adopt the sequence illustrated in Fig. S8. First, the phonon mode is prepared in state $|1\rangle$ or $(|0\rangle + |1\rangle)/\sqrt{2}$ by swapping the corresponding qubit states $|\uparrow\rangle$ or $(|\downarrow\rangle + |\uparrow\rangle)/\sqrt{2}$ with the phonon ground state through the resonant Jaynes–Cummings interaction. Then, the system evolves freely for a variable time interval t , after which a Wigner function measurement is performed. The latter consists of a displaced parity measurement, where a displacement of the phonon mode $D(\beta)$ is followed by a parity measurement implemented through a strong dispersive interaction between the qubit and the phonon [14].

The above sequence results in a single measurement of the parity at point $-\beta$ in phase space. The value of the Wigner function is then obtained by averaging $\sim 4 \cdot 10^3$ of such parity measurements. Finally, to record a two-dimensional Wigner function like the ones in Fig. 2, we repeat the described procedure for many different values of β .

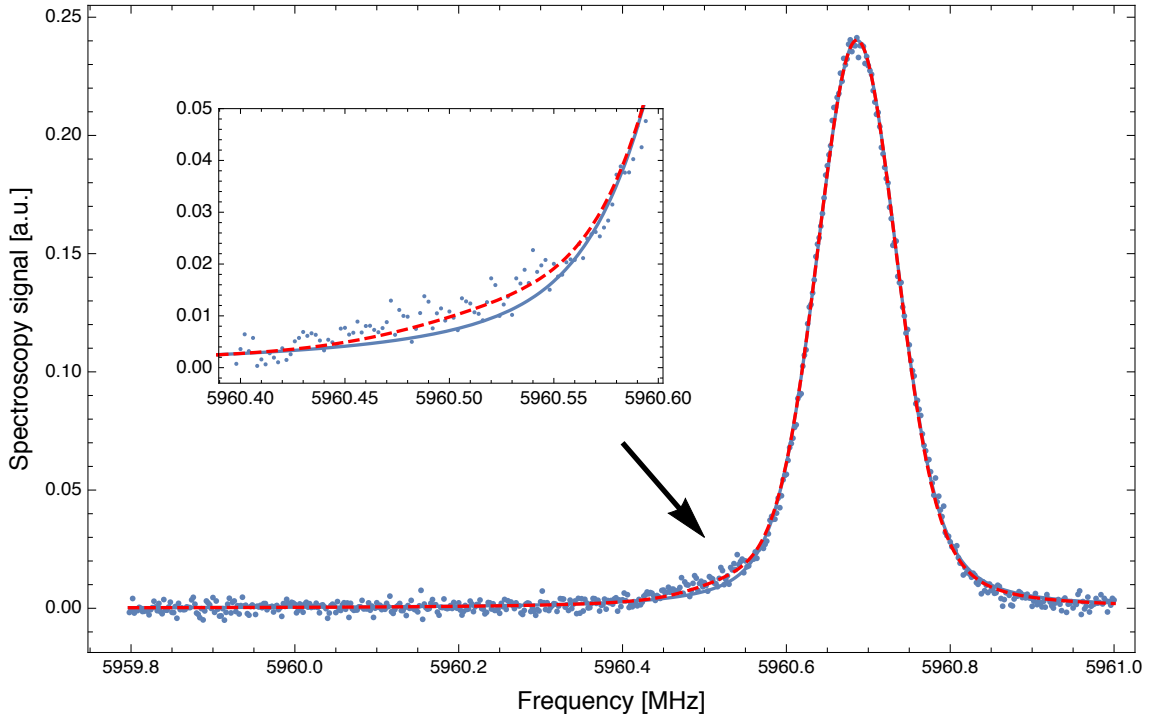


FIG. S7. Phonon mode thermometry. Spectroscopy of the qubit resonance frequency, while coupled to the phonon mode in the strong dispersive regime. In this regime, the qubit frequency depends on the phonon occupation number. Observing an asymmetry in the measured curve thus indicates a non-zero phonon number, that we associate to an effective temperature (see text for details).

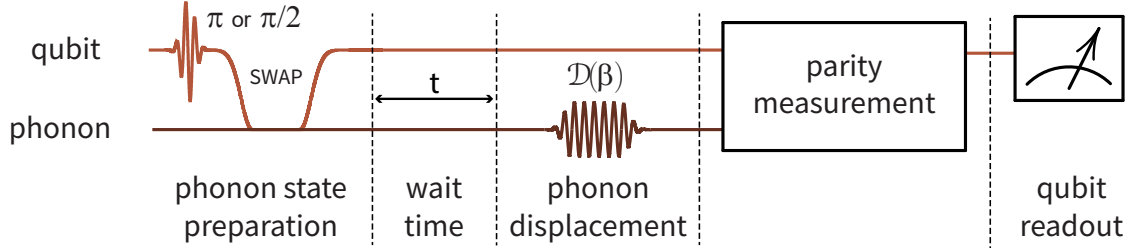


FIG. S8. Wigner function measurement of the time-evolved state. The experimental sequence used to record the data in Fig. 2 consists of the following steps: 1) phonon state preparation, 2) wait time t , and 3) displaced parity measurement. Further details about the parity measurement sequence are given in Ref. [14].

Supplementary Section F: Non-interferometric thermalization test

A straightforward and widely used approach to study collapse models are so-called non-interferometric tests, which focus on monitoring the noise or the energy changes in the studied system [21]. This puts bounds on modifications to quantum mechanics without the need of preparing a quantum state. In our experiment, we can do a similar analysis by monitoring the resonator occupation number. The Wigner function evolution under relaxation at the rate γ_{\downarrow} and macrorealistic diffusion predicts a steady-state energy $E_{\text{therm}} = \hbar\omega(1 + 2\Gamma/\gamma_{\downarrow})/2$. Hence, by measuring the steady state phonon population, we impose bounds on the hypothetical diffusion rate Γ .

To improve the bounds resulting from this analysis, one could also take into account additional known decoherence processes and a finite temperature characterized from independent measurements. Instead, we follow the most conservative estimation: we attribute all diffusion effects to the macrorealistic modification, thus overestimating its effect and underestimating the resulting bounds. Then the equilibrium temperature $T_{\text{therm}} = \hbar\omega\Gamma/\gamma_{\downarrow}k_B$ is a result of the competing relaxation rate γ_{\downarrow} and macrorealistic diffusion rate Γ . The decay rate γ_{\downarrow} can be reliably measured far from equilibrium by preparing a thermal state at $T(t=0) \gg T(t=\infty) = T_{\text{therm}}$ and verifying a constant decay rate. This leaves only one free parameter Γ to estimate, which then gives non-interferometric exclusion bounds on collapse models based on the observed amount of classical heating.

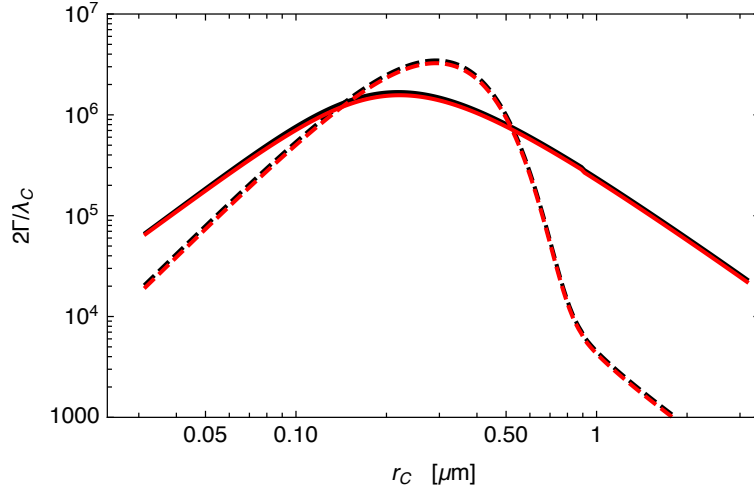


FIG. S9. Comparison between diffusion rates. Our results (red), compared to the results of Ref. [23] (black). Solid curve is for a mode index of $\ell = 1$, while the dashed curve is for $\ell = 40$. We chose to plot $2\Gamma = 2\eta x_0^2$ for a direct comparison.

With the maximum dimensionless diffusion rate $\Gamma_{\max} = 3.5 \cdot 10^{13}/\tau_e$ and a thermal population of 1.6%, this analysis leads to $\Gamma = 0.016\gamma_{\downarrow}$. The measured $\gamma_{\downarrow} \approx 1/T_1$ then results in an exclusion of $\tau_e < 1.9 \cdot 10^{11}$ s at the length scale $\hbar/\sigma_q = 5 \cdot 10^{-7}$ m. This is weaker than other non-interferometric collapse tests performed with *ad hoc* experiments [21], or with large-scale endeavors like the LISA pathfinder experiment [32, 33], but it could be further improved by carefully optimizing the HBAR device geometry and the experimental sequences. Note however that no genuine quantum feature is actually verified in a collapse test based on classical noise bounds, meaning that it does not qualify for a benchmark based on the macroscopicity of a superposition.

Finally, as a side remark, let us mention that a new approach for performing non-interferometric tests of collapse models using bulk resonators has been recently proposed in Ref. [23]. Our analytical results can readily be applied to this proposal, leading to an exact expression of the diffusion rate. Given the mode function $u(\mathbf{r}) = \cos(\pi\ell x/L)\mathbf{e}_x$ hosted by a homogeneous cylinder of radius R and length L , we obtain the diffusion rate

$$\Gamma = \lambda_C \frac{x_0^2 \bar{\rho}^2 \pi^2 r_C^5 R^2}{2m_e^2 L^3} \left[\frac{\exp(R^2/2r_C^2) - I_0(R^2/2r_C) - I_1(R^2/2r_C)}{\exp(R^2/2r_C^2)} \right] \times \left[-\ell\pi\hbar(L/\sqrt{2}r_C, 0, n) + \sqrt{2} \left((-1)^n e^{-L^2/4r_C^2} - 1 \right) \sigma_L \left(\ell^2 \pi^2 - L^2/r_C^2 \right) + (-1)^n \ell \pi^2 \text{Re} \left\{ h(L/\sqrt{2}r_C, L/\sqrt{2}r_C, \ell) \right\} \right]. \quad (\text{F1})$$

For convenience, we have adopted the parameter notation of the CSL collapse model here, $\lambda_C = m_0^2/m_e^2\tau_e$ and $r_C = \hbar/\sqrt{2}\sigma_q$. Our formula must be multiplied by two for direct comparison with the approximate momentum diffusion rate term given by the authors,

$$2\Gamma \approx \lambda_C \frac{x_0^2 r_C^3 \bar{\rho}^2 R^2}{2m_0^2} \left(\frac{64\sqrt{\pi}}{L/\ell} \right) \left[\frac{\exp(R^2/2r_C^2) - I_0(R^2/2r_C) - I_1(R^2/2r_C)}{2\exp(R^2/2r_C^2)} \right] \times \int_{-\infty}^{\infty} da \exp\left(-r_C^2 \left(\frac{2\pi a}{L/\ell}\right)^2\right) \frac{(-8 + (8 + a^2\pi^2)\cos(a\pi/2))^2 \sin^2(\ell\pi a/2)}{4a^2\pi^2 \cos^2(\pi a/2)}. \quad (\text{F2})$$

A comparison between both expressions is shown in Fig. S9 for the parameters chosen in Ref. [23], $\bar{\rho} = 3210 \text{ kg m}^{-3}$, $R = 35 \mu\text{m}$, $\omega = 2\pi \times 6.33 \text{ Hz}$, and for the two settings at $\ell = 1$, $L = 1.5 \mu\text{m}$ and at $\ell = 40$, $L = 60 \mu\text{m}$, showing good agreement.

-
- [1] M. Schlosshauer, Quantum decoherence, *Phys. Rep.* **831**, 1 (2019).
- [2] A. J. Leggett, Testing the limits of quantum mechanics: motivation, state of play, prospects, *J. Phys.: Condens. Matter* **14**, R415 (2002).
- [3] T. Kovachy, P. Asenbaum, C. Overstreet, C. A. Donnelly, S. M. Dickerson, A. Sugarbaker, J. M. Hogan, and M. A. Kasevich, Quantum superposition at the half-metre scale, *Nature* **528**, 530 (2015).
- [4] S. Abend, M. Gebbe, M. Gersemann, H. Ahlers, H. Müntinga, E. Giese, N. Gaaloul, C. Schubert, C. Lämmerzahl, W. Ertmer, W. P. Schleich, and E. M. Rasek, Atom-chip fountain gravimeter, *Phys. Rev. Lett.* **117**, 203003 (2016).
- [5] P. Asenbaum, C. Overstreet, T. Kovachy, D. D. Brown, J. M. Hogan, and M. A. Kasevich, Phase shift in an atom interferometer due to spacetime curvature across its wave function, *Phys. Rev. Lett.* **118**, 183602 (2017).
- [6] V. Xu, M. Jaffe, C. D. Panda, S. L. Kristensen, L. W. Clark, and H. Müller, Probing gravity by holding atoms for 20 seconds, *Science* **366**, 745 (2019).
- [7] S. Eibenberger, S. Gerlich, M. Arndt, M. Mayor, and J. Tüxen, Matter–wave interference of particles selected from a molecular library with masses exceeding 10000 amu, *Phys. Chem. Chem. Phys.* **15**, 14696 (2013).
- [8] Y. Y. Fein, P. Geyer, P. Zwick, F. Kiałka, S. Pedalino, M. Mayor, S. Gerlich, and M. Arndt, Quantum superposition of molecules beyond 25 kda, *Nat. Phys.* **15**, 1242 (2019).
- [9] B. A. Stickler, B. Papendell, S. Kuhn, B. Schriniski, J. Millen, M. Arndt, and K. Hornberger, Probing macroscopic quantum superpositions with nanorotors, *New J. Phys.* **20**, 122001 (2018).
- [10] R. Kaltenbaek *et al.*, Research campaign: Macroscopic quantum resonators (MAQRO), *Quantum Sci. Technol.* **10.1088/2058-9565/aca3cd** (2022).
- [11] Y. Chu, P. Kharel, T. Yoon, L. Frunzio, P. T. Rakich, and R. J. Schoelkopf, Creation and control of multi-phonon Fock states in a bulk acoustic-wave resonator, *Nature* **563**, 666 (2018).
- [12] K. J. Satzinger, Y. P. Zhong, H. S. Chang, G. A. Peairs, A. Bienfait, M.-H. Chou, A. Y. Cleland, C. R. Conner, É. Dumur, J. Grebel, I. Gutierrez, B. H. November, R. G. Povey, S. J. Whiteley, D. D. Awschalom, D. I. Schuster, and A. N. Cleland, Quantum control of surface acoustic-wave phonons, *Nature* **563**, 661 (2018).
- [13] E. A. Wollack, A. Y. Cleland, R. G. Gruenke, Z. Wang, P. Arrangoiz-Arriola, and A. H. Safavi-Naeini, Quantum state preparation and tomography of entangled mechanical resonators, *Nature* **604**, 463 (2022).
- [14] U. von Lüpke, Y. Yang, M. Bild, L. Michaud, M. Fadel, and Y. Chu, Parity measurement in the strong dispersive regime of circuit quantum acoustodynamics, *Nat. Phys.* **18**, 794 (2022).
- [15] M. Bild, M. Fadel, Y. Yang, U. von Lüpke, P. Martin, A. Bruno, and Y. Chu, Schrödinger cat states of a 16-microgram mechanical oscillator, *arXiv preprint arXiv:2211.00449* (2022).
- [16] S. Nimmrichter and K. Hornberger, Macroscopicity of mechanical quantum superposition states, *Phys. Rev. Lett.* **110**, 160403 (2013).
- [17] B. Schriniski, S. Nimmrichter, B. A. Stickler, and K. Hornberger, Macroscopicity of quantum mechanical superposition tests via hypothesis falsification, *Phys. Rev. A* **100**, 032111 (2019).
- [18] Note that the macrorealist modification hypothesis can be probed also in experiments that do not involve quantum superpositions. Only observations of genuine quantum signatures can therefore be assigned a benchmark value μ [17]. This requires the interrogated state not to have an underlying classical description, excluding all oscillator states with positive Wigner function.
- [19] A. Royer, Wigner function as the expectation value of a parity operator, *Phys. Rev. A* **15**, 449 (1977).
- [20] A. Bassi, K. Lochan, S. Satin, T. P. Singh, and H. Ulbricht, Models of wave-function collapse, underlying theories, and experimental tests, *Rev. Mod. Phys.* **85**, 471 (2013).
- [21] M. Carlesso, S. Donadi, L. Ferioldi, M. Paternostro, H. Ulbricht, and A. Bassi, Present status and future challenges of non-interferometric tests of collapse models, *Nat. Phys.* **18**, 243 (2022).
- [22] See Supplementary Information for details on the experimental setup and the theoretical calculations, including Refs. [27–33].
- [23] G. Tobar, S. Forstner, A. Federov, and W. P. Bowen, Testing spontaneous wavefunction collapse with quantum electromechanics, *arXiv preprint arXiv:2206.14531* (2022).
- [24] Y. Seis, T. Capelle, E. Langman, S. Saarinen, E. Planz, and A. Schliesser, Ground state cooling of an ultracoherent electromechanical system, *Nat. Comm.* **13**, 1507 (2022).
- [25] This rough estimate is based on [17], by approximating the mode in [24] as the fundamental Bessel mode $u(\mathbf{r}) = J_0(4.81 \sqrt{y^2 + z^2}/d)\mathbf{e}_x$, for a disc with diameter $d = 100 \mu\text{m}$, 14 nm thickness, and $m_{\text{eff}} \approx 68 \text{ pg}$. Precise μ -values would depend on a combination of effective mass, mode profile, and observed duration of Wigner negativities.
- [26] B. Schriniski, S. Nimmrichter, and K. Hornberger, Quantum-classical hypothesis tests in macroscopic matter-wave interferometry, *Phys. Rev. Res.* **2**, 033034 (2020).
- [27] H. Jeffreys, An invariant form for the prior probability in estimation problems, *Proc. R. Soc. Lond. A* **186**, 453 (1946).
- [28] P. Arrangoiz-Arriola, *Quantum acoustics with lithium niobate nanostructures*, *Ph.D. thesis*, Stanford University (2019).
- [29] K. J. Satzinger, *Quantum control of surface acoustic wave phonons*, *Ph.D. thesis*, UC Santa Barbara (2018).
- [30] K. J. Satzinger, private communication.
- [31] Y. Chu, P. Kharel, W. H. Renninger, L. D. Burkhardt, L. Frunzio, P. T. Rakich, and R. J. Schoelkopf, Quantum acoustics with superconducting qubits, *Science* **358**, 199 (2017).
- [32] M. Armano, H. Audley, G. Auger, J. Baird, M. Bassan, P. Binetruy, M. Born, D. Bortoluzzi, N. Brandt, M. Caleno, *et al.*, Sub-femto-g free fall for space-based gravitational wave observatories: Lisa pathfinder results, *Phys. Rev. Lett.* **116**, 231101 (2016).
- [33] M. Carlesso, A. Bassi, P. Falferi, and A. Vinante, Experimental bounds on collapse models from gravitational wave detectors, *Phys. Rev. D* **94**, 124036 (2016).